Soft Matter

PAPER

View Article Online
View Journal | View Issue

Cite this: *Soft Matter*, 2018, **14**, 2465

Towards the colloidal Laves phase from binary hard-sphere mixtures *via* sedimentation

Tonnishtha Dasgupta and Marjolein Dijkstra*

Received 1st February 2018,
Accepted 15th March 2018

DOI: 10.1039/c8sm00237a

rsc.li/soft-matter-journal

Colloidal photonic crystals, which show a complete band gap in the visible region, have numerous applications in fibre optics, energy storage and conversion, and optical wave guides. Intriguingly, two of the best examples of photonic crystals, the diamond and pyrochlore structure, can be self-assembled into the colloidal $MgCu_2$ Laves phase crystal from a simple binary hard-sphere mixture. For these colloidal length scales thermal and gravitational energies are often comparable and therefore it is worthwhile to study the sedimentation phase behavior of these systems. For a multicomponent system this is possible through a theoretical construct known as a stacking diagram, which constitutes a set of all possible stacking sequences of phases in a sedimentation column, and uses as input the bulk phase diagram of the system in the chemical potential plane. We determine the stable phases for binary hard-sphere systems with varying diameter ratios using Monte Carlo simulations and analytical equations of state available in literature and calculate the corresponding stacking diagrams. We also discuss observations from event-driven Brownian dynamics simulations in relation to our theoretical stacking diagrams.

1 Introduction

Colloidal particles can serve as physical models for atomic systems in that they can crystallize into periodic, ordered phases which are analogous to atomic crystals. The best known example of this, first reported by simulations[1] and followed up later by experiments,[2] is the formation of the face-centered-cubic (fcc) crystal phase, which crystallizes from a colloidal hard-sphere fluid. As the length and time scales of colloidal systems are easier to study experimentally than their atomic counterparts, these systems can provide valuable fundamental insights into physical processes such as crystallization and phase transitions.[3,4]

A significant application of colloidal particles is to serve as building blocks for photonic crystals. Photonic crystals can control the propagation of light by virtue of their periodically varying refractive index or dielectric contrast. With lattice constants of the same order as the wavelength of light, these materials show a photonic band gap for certain light frequencies. Photonic bandgap materials have a broad range of applications such as optical wave guides,[5] sensors[6] and in energy storage[7] /conversion[8] among others. A complete photonic bandgap may be shown by a three-dimensional photonic crystal which prevents the propagation of specific wavelengths of light in all directions. With colloids as building blocks, photonic crystals can open up a band gap in the visible range of frequencies,[9] depending on their refractive index, packing geometry and density. In particular, the diamond[10] and pyrochlore[11] structures have been known to open up a wide photonic band gap even at low refractive indices, thereby making their photonic properties robust to defects.[12] The colloidal diamond and pyrochlore crystals are open structures with a low packing fraction rendering them entropically unfavourable and mechanically unstable. This problem is circumvented by the fact that these two structures make up the large (Mg) and small (Cu) species counterparts of the colloidal $MgCu_2$ Laves phase, respectively, which is the thermodynamically stable phase for a simple binary hard-sphere colloidal mixture in the diameter ratio range of 0.76 to 0.84.[13] By removing the particles on one of the sublattices the photonic open structures can subsequently be retrieved.

In order for the $MgCu_2$ Laves phase to possess an optical band gap for one of its sublattices, the spheres must be on the colloidal length scale, which corresponds to a regime where the thermal and gravitational energies of the particles are comparable. Therefore it is important to account for gravity while studying the self-assembly of the stable colloidal Laves phase. The competition between thermal and gravitational forces leads to a sedimentation–diffusion equilibrium, which we study in this work. For a one-component colloidal system under gravity, it is fairly straightforward to obtain information about the bulk thermodynamics of the system from its sedimentation behavior.[14,15] For this, one simply needs to calculate the height-dependent density profile and invert it to calculate the osmotic pressure at every point along the sedimentation column. In this way, a single experiment/simulation

Soft Condensed Matter, Debye Institute for Nanomaterials Science, Department of Physics, Utrecht University, Princetonplein 1, 3584 CC, Utrecht, The Netherlands. E-mail: m.dijkstra@uu.nl; Tel: +31 (0)30 253 3270

can yield the entire equation of state, *i.e.* the pressure as a function of density. However, for systems with more than one component, correlating bulk thermodynamics to the sedimentation–diffusion equilibria is not trivial. In this case, the bulk phase diagram (in the absence of gravity) is converted to an alternate phase space which accounts for gravity. This constructed phase space is known as a stacking diagram.[16,17]

A stacking diagram (SD) is a set of all possible stacking sequences of phases found in a sedimentation column. A stacking sequence indicates the phases observed sequentially from the bottom to the top of a sedimentation column. The theory for calculating a SD takes as input a bulk phase diagram calculated in the chemical potential plane. The method to convert this into a stacking diagram involves a Legendre transformation to an alternate plane.[16] SDs can be used to predict various unexpected phenomena in sedimenting systems. For example, ''floating phases'' were observed in colloid-polymer mixtures, where a floating colloid-rich liquid slab was sandwiched between two polymer-rich colloidal gas slabs,[18] and ''floating hexagonal crystal phases'' have been reported in simulations of colloidal spheres with a soft corona.[19] A reentrant percolating network in a patchy colloidal mixture was both predicted and observed in simulations.[20] In another example, a floating nematic phase suspended on an isotropic phase was observed in an experimental system of colloidal platelets and spheres.[21] This observation was backed up by a stacking diagram which showed floating phases in certain stacking sequences. This demonstrates the power of this simple but predictive theory in bridging the gap between theory and experiments and asserts the importance of constructing SDs.

In a recent work, the $MgCu_2$ Laves phase was reported to be thermodynamically stable for a hard sphere–hard tetramer mixture.[22] This was based on the idea that the pyrochlore structure can be grouped into tetrahedral clusters of spheres. Following a similar logic of building blocks, an experimental system of DNA-coated spheres and preassembled tetrahedral clusters was used in a recent work to obtain the $MgCu_2$ Laves phase.[23] However, this system used DNA-mediated short-ranged attractions between the unlike species to promote self-assembly and the $MgCu_2$ Laves structure was not observed for tetrahedral clusters made of non-overlapping adjacent spheres. As hard-sphere colloids are notably experimentally realizable and the tunability of their length scales is well within control to suit various photonic applications, it is worthwhile to study the sedimentation phase behavior of this system.

In this work we study the sedimentation–diffusion equilibria of binary colloidal hard-sphere mixtures, where the spheres interact only through hard-core interactions, by constructing stacking diagrams. We calculate SDs for a diameter ratio of 0.85, for which the Laves phase is not stable, and 0.82, which shows an entrant stable binary Laves phase. We first calculate the bulk phase diagrams in the pressure–composition (most common), packing fraction (experimentally significant) and chemical potential (for constructing SDs) representations. We note that these phase diagrams have already been reported but solely in the pressure–composition and packing fraction representation.[13,24] In order to construct the stacking diagrams, we need the phase diagrams in the chemical potential plane. We therefore repeat these calculations in order to determine the phase diagrams in the chemical potential plane. We then determine the SDs which show the different stacking sequences of phases (as seen in the bulk phase diagrams) under a gravitational field for a range of gravitational lengths, bulk compositions and bulk concentrations. We then perform event-driven Brownian dynamics simulations for selected state points in the SD corresponding to a size ratio of 0.82 and discuss the sedimentation behavior observed in relation to our theoretical predictions.

2 Methodology

2.1 Bulk phase behaviour of binary hard-sphere systems

The first step towards studying the sedimentation–diffusion equilibrium of a binary mixture of large hard spheres with diameter σ_L and small hard spheres with diameter σ_S is to ascertain the bulk thermodynamics of the system, *i.e.*, the phase behavior in the absence of gravity. Therefore we first calculate the bulk phase diagram for a specific diameter ratio $q = \sigma_S/\sigma_L$, which describes the coexistence between different phases for this system. Coexistence between phase α and β is calculated using the mechanical equilibrium condition, $P^\alpha = P^\beta$, with P the pressure, and employing the chemical or diffusive equilibrium condition for both the large and small species, $\mu_L^\alpha = \mu_L^\beta$ and $\mu_S^\alpha = \mu_S^\beta$, respectively, with μ_L (μ_S) the chemical potential of the large (small) species. The chemical potential equivalence criteria dictate that we construct common tangents on the Gibbs free energy G – composition x plane at a fixed pressure P. Here, we define $x_S = N_S/N$ with $N = N_S + N_L$ and N_S (N_L) the number of small (large) hard spheres. From this technique, we can directly obtain the coexistence species compositions at each pressure and calculate other coexistence properties on the packing fraction ($\eta_L = \pi\sigma_L{}^3N_L/6V - \eta_S = \pi\sigma_S{}^3N_s/6V$) representation with V the volume of the system, or on the chemical potential (μ_L–μ_S) plane. In order to obtain the Gibbs free energy $G = F + PV$, we first calculate the Helmholtz free energies F of the different fluid and solid phases. The solid phases that we consider are the face-centered-cubic (fcc) crystals formed of purely large or small hard-sphere species and the Laves phase, and ignore hereby the substitutional solid solutions of the fcc and Laves phases. We employ analytical expressions from literature for the Helmholtz free energy of a binary hard-sphere fluid,[25] and we employ the Speedy equation of state[26] for the pure fcc phases.

In order to obtain the Helmholtz free energy as a function of density $\rho = N/V$, we integrate the equation of state from a reference density ρ_0

$$\frac{\beta F(\rho)}{N} = \frac{\beta F(\rho_0)}{N} + \int_{\rho_0}^{\rho} \mathrm{d}\rho' \frac{\beta P(\rho')}{\rho'^2}, \quad (1)$$

where $\beta = 1/k_BT$, k_B denotes the Boltzmann constant, and T the temperature. To determine the equation of state of the Laves phases, we perform Monte Carlo simulations in the *NPT* ensemble.

The Helmholtz free energy $F(\rho_0)$ of the fcc and Laves phases at a reference density ρ_0 is calculated using the Frenkel–Ladd method in Monte Carlo simulations in the *NVT* ensemble, which involves an Einstein integration of a system of non-interacting particles that are connected to the lattice positions of an ideal crystal phase *via* harmonic springs

$$\beta U_\lambda(\mathbf{r}^N) = \beta U(\mathbf{r}^N) + \lambda \sum_{i=1}^{N} (\mathbf{r}_i - \mathbf{r}_{0,i})^2 \Big/ {\sigma_L}^2. \tag{2}$$

Here $U(\mathbf{r}^N)$ is the potential energy of the system due to the hard-sphere interactions, $\mathbf{r}_{0,i}$ denotes the ideal lattice position of particle i in the crystal of interest, and λ is a dimensionless coupling parameter, which goes from 0, corresponding to the interacting system of interest for which we want to compute the free energy, to λ_{max}, which corresponds to an Einstein crystal, where the spring constant is chosen sufficiently large that the particles do not interact with each other.

The Helmholtz free energy is obtained from[27,28]

$$\begin{aligned}\frac{\beta F(N,V,T)}{N} = {} & \frac{\beta U(\mathbf{r}_0^N)}{N} + \frac{3(N-1)}{2N}\ln\left(\frac{\Lambda^2\lambda_{max}}{\pi{\sigma_L}^2}\right) \\ & + \frac{1}{N}\ln\left(\frac{N\Lambda^3}{V}\right) - \frac{3}{2N}\ln(N) \\ & - \frac{1}{N}\int_{\ln c}^{\ln(\lambda_{max}+c)} (\lambda + c)\left\langle \sum_{i=1}^{N} \frac{(\mathbf{r}_i - \mathbf{r}_{0,i})^2}{{\sigma_L}^2} \right\rangle_\lambda^{CM} \\ & \times \mathrm{d}[\ln(\lambda + c)],\end{aligned} \tag{3}$$

where $U_\lambda(\mathbf{r}_0^N)$ is the potential energy when all particles are at their ideal lattice positions, Λ is the thermal wavelength, $\langle\cdots\rangle_\lambda^{CM}$ denotes that the ensemble average is sampled for a solid with a fixed center of mass using the Boltzmann factor $\exp(-\beta U_\lambda)$, and

$$c = \frac{1}{\left\langle \sum_{i=1}^{N} (\mathbf{r}_i - \mathbf{r}_{0,i})^2 \Big/ {\sigma_L}^2 \right\rangle_0^{CM}}. \tag{4}$$

The integral is calculated numerically using a 20-point Gauss–Legendre quadrature.

2.2 Accounting for gravity

Once we have ascertained the bulk thermodynamics, we study this binary system sedimenting under gravity. To this end, we construct a stacking diagram, which is the set of all possible sequences of phases stacked in a sedimentation column.

The theory behind the construction of a stacking diagram[16] is based on the chemical potentials of the two species. Once gravity is "switched on", a non-trivial density and composition profile is obtained along the direction of gravity z of the sedimentation column. We define a local chemical potential $\mu_i(z)$ of species i, which varies linearly with height z along the sedimentation column

$$\mu_i(z) = \mu_i^0 - m_i g z \tag{5}$$

where μ_i^0 is the chemical potential of species i in the absence of gravity, m_i is the buoyant mass of particle species i, and g is the gravitational acceleration. Eliminating the z-dependence, we obtain a linear relation between the local chemical potentials of the large (μ_L) and small spheres (μ_S).

$$\mu_S(\mu_L) = a + s\mu_L, \tag{6}$$

where the slope s of the sedimentation path is given by the ratio of the buoyant masses

$$s = \frac{m_S}{m_L}, \tag{7}$$

and a denotes the composition variable, which is a function of the initial composition and concentration of the system[16,29]

$$a = \mu_S^0 - s\mu_L^0. \tag{8}$$

For low Peclet numbers, *i.e.*, in the case of slowly varying inhomogeneities, we assume that the local density approximation (LDA) is valid. This approximation implies that the local chemical potential $\mu_i(z)$ of species i is equal to the chemical potential μ_i of a corresponding equilibrium bulk reservoir. The significance of the LDA is that the correlation between gravitational variable s and composition variable a now appears as a straight line (eqn (6)) on the bulk phase diagram in the plane of chemical potentials μ_L–μ_S. This straight line is called a "sedimentation path" and the set of all such paths constitutes a stacking diagram. The point at which a sedimentation path intersects with a bulk binodal represents a phase transition. Therefore, each sedimentation path corresponds to a specific stacking sequence of phases in the corresponding stacking diagram.

2.3 Event-driven Brownian dynamics simulations

Once we have mapped out the stacking diagrams of a binary mixture of hard spheres, we perform event-driven Brownian dynamics (EDBD) simulations[30,31] at selected state points for such a mixture sedimenting under gravity on a hard wall. We carry out simulations on a binary system of N hard-sphere colloids with a diameter ratio $q = 0.82$ in a volume V in the *NVT* ensemble. The gravitational field is directed along the z-axis and each colloid i is subjected to an external potential $U(z_i) = m_i g z_i$ where g is the acceleration due to gravity, m_i is the buoyant mass of particle i, and z_i is the vertical coordinate of colloid i. Two hard walls are placed at $z = 0$ and $z = H - \sigma_L$. The simulation method considers particle collisions (with the wall and each other) as discrete events and progresses through a sequence of collision time intervals to the nearest event calculated through the Newtonian equations of motion. During the simulation, particle velocities are stochastically and periodically adjusted at a regular interval of Δt to account for the Brownian "kicks" from the surrounding solvent

$$\mathbf{v}(t + \Delta t) = \alpha_t \mathbf{v}(t) + \beta_t \mathbf{v}_R(t), \tag{9}$$

where $\mathbf{v}(t + \Delta t)$, $\mathbf{v}(t)$ are the particle velocities before and after the Brownian adjustment, $\mathbf{v}_R(t)$ is a variable calculated from a 3D Gaussian distribution with mean 0 and variance $k_B T/m_i$. We set $\alpha_t = 1/\sqrt{2}$ with a probability $\nu\Delta t$ and 1 otherwise. We employ

$\beta_t = \sqrt{1-\alpha_t^2}$ in order to keep the temperature constant. Following ref. 31, we set $\nu = 10\tau^{-1}$ and $\Delta t = 0.01\tau$ in all our simulations and use $\tau = \sqrt{m_L/k_B T}\sigma_L$ as the time unit of our simulations. We remark that τ is different from the Brownian time unit τ_B used in ref. 31. The details of the EDBD simulations are elaborately described in ref. 31 and 32.

The parameter that describes the effect of gravity on sedimenting colloids is the gravitational length given as $l_g^i = k_B T/m_i g$, which corresponds to the height difference over which the gravitational energy of colloid i is comparable to the thermal energy.[15] The dimensionless parameter of interest is the gravitational Peclet number which is given by $\mathrm{Pe}_i = \sigma_i/l_g^i$. In this work, we show simulation results for a binary mixture of hard spheres with a diameter ratio $q = 0.82$, and three different gravitational length ratios $(l_g^L/l_g^S) = 0.4$, 0.68 and 1.0, corresponding to specific points in the stacking diagram.

3 Results and discussion

We first calculate the bulk phase diagrams for two diameter ratios, $q = 0.85$, for which the Laves phase is not stable, and $q = 0.82$, for which the phase diagram exhibits a stable Laves phase as shown in ref. 24. Subsequently, we determine the bulk phase diagrams in the large-sphere chemical potential μ_L–small-sphere chemical potential μ_S representation in order to determine the stacking diagrams of these systems that represent the different stacking sequences of phases in a sedimentation–diffusion equilibrium. We will first present our results for $q = 0.85$ and, subsequently, we will describe our findings for $q = 0.82$.

3.1 Bulk phase diagram for $q = 0.85$

Using the method described in Section 2.1, we calculate the bulk phase diagram for $q = 0.85$. In Fig. 1, we present the bulk phase diagram in the pressure $\beta P\sigma_L{}^3$–composition x_S representation, where x_S refers to the number fraction of small spheres. We observe three thermodynamically stable phases, the pure fcc of large spheres ($\mathrm{fcc_L}$), pure fcc of small spheres ($\mathrm{fcc_S}$), and the binary fluid mixture. The phase diagram exhibits a fluid–$\mathrm{fcc_L}$, a fluid–$\mathrm{fcc_S}$, and a $\mathrm{fcc_S}$–$\mathrm{fcc_L}$ coexistence region. The Laves phase is unstable at all pressures. At pressures $\beta P\sigma_L{}^3 \leq 11.5$, the fluid phase is stable. In the range $11.5 \leq \beta P\sigma_L{}^3 \leq 24.65$, we observe two coexistence regimes. For composition $x_S > 0.7$, the fcc of small spheres ($\mathrm{fcc_S}$) coexists with the fluid phase and for $x_S < 0.7$, coexistence is found between the fcc of large spheres ($\mathrm{fcc_L}$) and the fluid phase. Interestingly, at pressures $\beta P\sigma_L{}^3 \geq 24.65$, we observe that the binary system demixes into two pure component fcc phases, which is to be expected as the phase-separated fcc phase yields the best packing for a binary mixture at this diameter ratio. A triple point between the three phases is observed at $\beta P\sigma_L{}^3 = 24.65$, at which all the three phases are in thermodynamic equilibrium. For experimentalists, a more appealing representation of the phase diagram is the plane of packing fractions of the individual species. We therefore also present the phase diagram in an η_L–η_S representation. This is shown in Fig. 2. One can observe that the triple point, which is a point in the $\beta P\sigma_L{}^3$–x_S plane where three coexistence binodals meet, appears as a triangular region in the η_L–η_S plane.

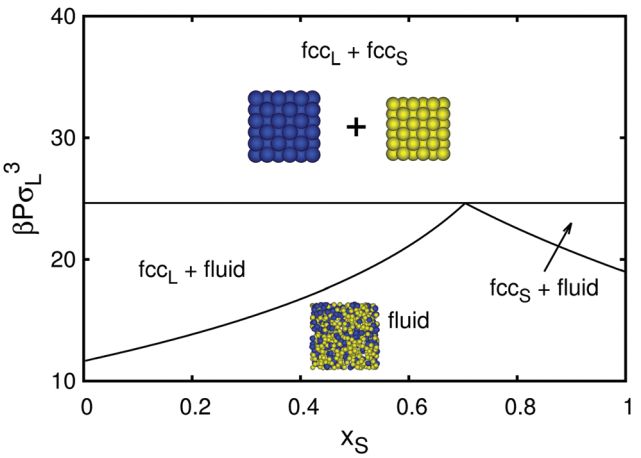

Fig. 1 Bulk phase diagram of a binary mixture of hard spheres with a diameter ratio $q = 0.85$ in the pressure $\beta P\sigma_L{}^3$–composition x_S representation.

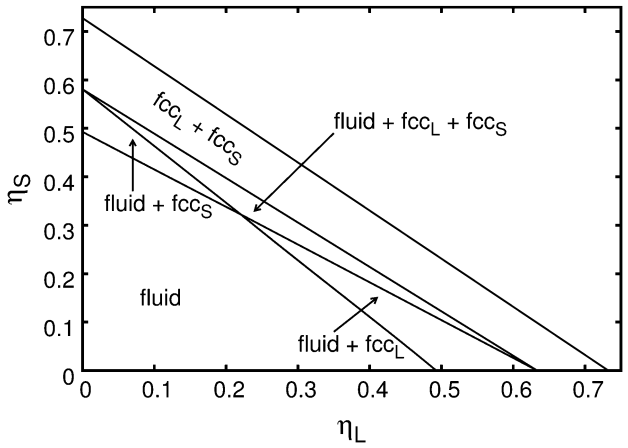

Fig. 2 Bulk phase diagram of a binary mixture of hard spheres with a diameter ratio $q = 0.85$ in the large-sphere packing fraction η_L–small-sphere packing fraction η_S representation.

3.2 Stacking diagram for $q = 0.85$

In the previous subsection, we calculated the bulk phase diagram of a binary hard-sphere mixture with a diameter ratio of $q = 0.85$. We now consider this system in a gravitational field. Following the formulation described in Section 2.2, we calculate the corresponding stacking diagram to describe the sedimentation–diffusion equilibria of this system. To calculate the stacking diagram, we first convert Fig. 1 to the chemical potential $(\mu_L$–$\mu_S)$ plane as shown in Fig. 3. Subsequently, the bulk phase diagram in the chemical potential plane can be converted to a stacking diagram in the a–s plane, which describes the different stacking sequences that can be observed in a sedimentation–diffusion equilibrium. The sedimentation paths, as described by $a = \mu_S - s\mu_L$, are drawn as colored dashed lines in the μ_L–μ_S phase diagram in Fig. 3. Each of these sedimentation paths corresponds to an

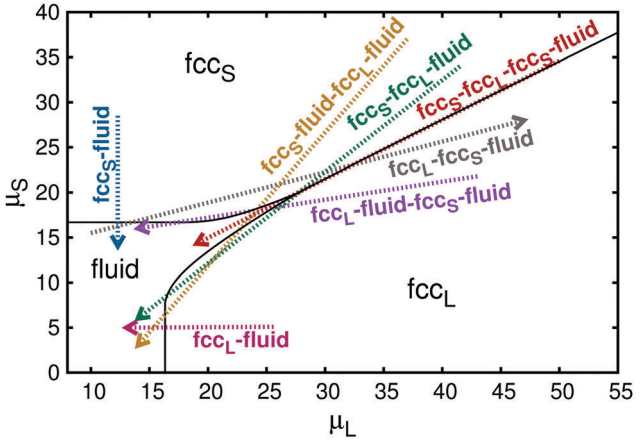

Fig. 3 Bulk phase diagram of a binary mixture of hard spheres with a diameter ratio q = 0.85 in the chemical potential of large spheres μ_L–chemical potential of small spheres μ_S representation. The solid lines represent the bulk binodals – each point on a binodal represents two phases in equilibrium with each other. The phase transition to the pure fcc of small and large spheres are shown by the horizontal and vertical asymptotic extensions of the respective binodals. The colored dashed lines represent typical sedimentation paths.

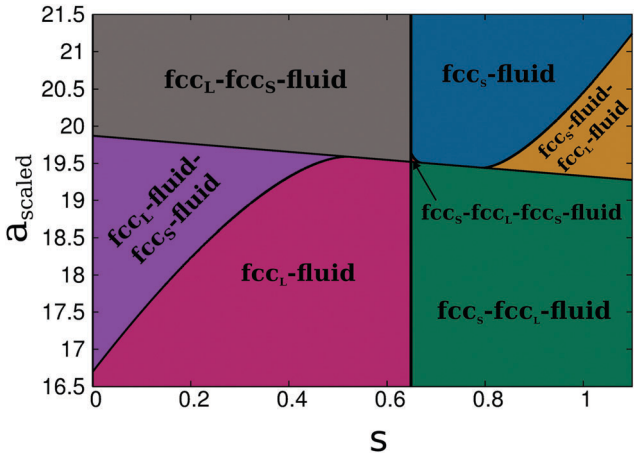

Fig. 4 The stacking diagram for a binary mixture of hard spheres with a diameter ratio q = 0.85. The colored regions represent the different stacking sequences of phases observed in a sedimentation column. The regions correspond to the similarly colored sedimentation paths shown in Fig. 3. For visualisation purposes, the a axis was linearly scaled with respect to s by a constant c. The new scaled $a_{scaled} = a - c \times s$ where $c = -27$.

unique stacking sequence and an unique point in the stacking diagram as shown in Fig. 4. Each region in the stacking diagram represents a collection of points with identical stacking sequences and the color of these regions corresponds to the color of the sedimentation paths drawn in the phase diagram in the chemical potential plane (Fig. 3). It is important to mention here that these sedimentation paths are considered infinite, therefore a pure component crystal will always be present at the bottom. In case we consider sedimentation paths that are bounded by a pressure at the bottom and at the top of the sample cell, the stacking diagram will be much richer.[33]

The stacking diagram as shown in Fig. 4 is divided into different regions which are delimited from each other through the following boundaries or features.

(1) Sedimentation binodal: this is the locus of all sedimentation paths which are tangential to a bulk binodal. In this case, we have three bulk binodals, a fluid–fcc$_L$, fluid–fcc$_S$, and fcc$_S$–fcc$_L$ binodal, and therefore three corresponding sedimentation binodals.

(2) Terminal lines: these lines represent sedimentation paths passing through any terminal point of a binodal. A terminal point may be a critical point, a triple point or indeed any point at which a binodal terminates. There is one triple point observed in the bulk phase diagram for this system – where the solid fcc$_L$ phase, solid fcc$_S$ phase and the binary fluid phase coexist. This triple point translates into a terminal line in the stacking diagram.

(3) Asymptotic terminal lines: the difference between terminal lines and asymptotic terminal lines is that the former appears when a binodal ends at finite chemical potentials and the latter corresponds to infinite chemical potentials of one or both of the species. For example, when the phase transition involves a pure component phase, the chemical potential of the absent species becomes $-\infty$. Therefore the fcc$_S$–fluid binodal tends to a horizontal asymptote in the μ_S–μ_L plane as the chemical potential of the absent large sphere species $\mu_L \to -\infty$. We remind the reader that the parameter s represents the slope of the tangent to the bulk binodal (eqn (6)) which in the above case corresponds to $s \to 0$. Therefore all sedimentation paths parallel to the horizontal asymptote on the μ_S–μ_L plane yield a vertical line at $s = 0$ in the corresponding stacking diagram as shown in Fig. 4. Similarly, a binodal that involves the pure phase of small spheres corresponds to a vertical asymptote in the μ_S–μ_L plane as the chemical potential $\mu_S \to -\infty$, and hence $s = -\infty$. The vertical line $s = -\infty$ for $\forall a$ is clearly beyond the scale of Fig. 4. In the limit of infinite pressure, $P \to \infty$, the binary mixture demixes into a pure large-sphere close-packed fcc phase with $\mu_L \to \infty$ and a pure small-sphere close-packed fcc phase with $\mu_S \to \infty$. However, as can be seen from Fig. 3, the slope of this asymptote in the μ_L–μ_S representation approaches a constant corresponding to a vertical line at $s \simeq 0.65$ in the SD of Fig. 4.

3.3 Bulk phase diagram for q = 0.82

Next, we map out the phase diagram for a binary hard-sphere mixture with a slightly smaller diameter ratio, *i.e.*, q = 0.82 instead of q = 0.85. We present the resulting phase diagram in the $\beta P\sigma_L^3$–x_S representation in Fig. 5, which displays a stable Laves phase. In particular, we observe a large fcc$_L$–Laves phase coexistence region for a composition $x_S < 0.667$ as well as an fcc$_S$–Laves phase coexistence region for $x > 0.667$ in the pressure range $23.08 \leq \beta P\sigma_L^3 \leq 56.5$, which lies in between the fluid–fcc$_L$, fluid–fcc$_S$, and the fcc$_L$–fcc$_S$ phase coexistence regions. Similar to q = 0.85, we find a stable fluid phase for $\beta P\sigma_L^3 \leq 11.5$ as expected as this transition point is solely determined by a system of pure hard spheres at $x_S = 0$. For a pressure range $11.5 \leq \beta P\sigma_L^3 \leq 23.08$, we observe phase coexistence between a fluid and an fcc phase of only large spheres for $x_S < 0.6608$. Correspondingly, for $21.25 \leq \beta P\sigma_L^3 \leq 24.35$ and $x_S > 0.835$,

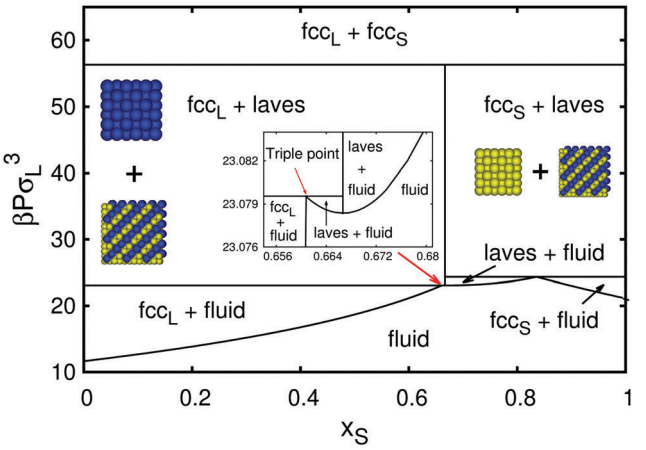

Fig. 5 Bulk phase diagram of a binary hard-sphere mixture with diameter ratio q = 0.82 in the pressure $\beta P\sigma_L^3$–composition x_S representation. The inset shows a zoom-in of the Laves–fcc$_L$–fluid triple point.

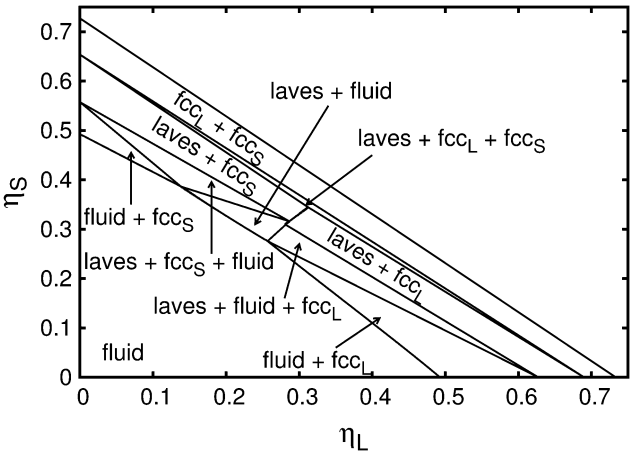

Fig. 6 Bulk phase diagram of a binary mixture of hard spheres with a diameter ratio q = 0.82 in the large-sphere packing fraction η_L–small-sphere packing fraction η_S representation.

the fluid phase coexists with an fcc phase of small spheres. Additionally, there is a coexistence region between the Laves phase and a fluid phase with a composition $0.667 < x_S < 0.835$ for $23.0783 \leq \beta P\sigma_L^3 \leq 24.35$, as well as an extremely narrow coexistence region between the Laves phase and fluid phase with $0.6608 < x_S < 0.667$ for $23.0783 \leq \beta P\sigma_L^3 \leq 23.0796$. The inset of Fig. 5 shows a zoom in of this part of the phase diagram. The latter coexistence region was missed in ref. 24. At pressures $\beta P\sigma_L^3 \geq 56.35$, we observe complete demixing of the two species into two pure fcc phases, fcc$_L$ and fcc$_S$, since this corresponds to the best packing with a packing fraction of $\eta_L = \eta_S \simeq 0.74$ at infinite pressures. It is worth noting that the Laves phase with a maximum packing fraction of $\eta \simeq 0.71$ is not the best-packed binary crystal structure at q = 0.82 as the αIrV, γCuTi, $AuTe_2$, and Ag_2Se phases have a higher maximum packing fraction than the Laves phase, but lower than the close-packed fcc phase.[13,24,34] Thus, for finite pressures, the stable crystal structures are not determined by maximum packing, but Gibbs free-energy calculations are required to determine the stable crystal phases.

To summarize, the presence of an additional thermodynamically stable Laves phase in the phase diagram of q = 0.82 in comparison to that of q = 0.85 results into 3 additional two-phase regions, *i.e.*, Laves–fluid, fcc$_L$–Laves, and fcc$_S$–Laves phase coexistences, as well as 3 triple points with either Laves–fcc$_L$–fcc$_S$, Laves–fcc$_S$–fluid, and Laves–fcc$_L$–fluid three-phase coexistence. For completeness, we also present the phase diagram in the η_L–η_S plane in Fig. 6 to facilitate comparison with experiments. The three triple points that are seen in Fig. 5 show up as triangular regions in Fig. 6.

3.4 Stacking diagram for q = 0.82

The appearance of an extra phase in the bulk phase diagram leads to a considerably more complicated stacking diagram. In order to determine the stacking diagram, we first convert the bulk phase diagram to the chemical potential μ_S–μ_L plane as shown in Fig. 7. We present the stacking diagram in the a–s representation in (Fig. 8). The stacking diagram is divided into

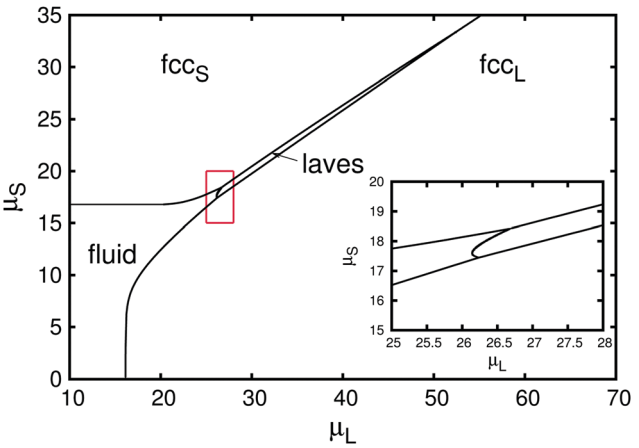

Fig. 7 Bulk phase diagram of a binary mixture of hard spheres with a diameter ratio q = 0.82 in the chemical potential of large spheres μ_L–chemical potential of small spheres μ_S representation. The solid lines represent the bulk binodals. The phase transition to the pure fcc of small and large spheres are shown by the horizontal and vertical asymptotic extensions of the respective binodals. The inset shows a zoom-in of the two triple points.

different regions that are delimited from each other through the following boundaries or features.

(1) Sedimentation binodal: in this case, we have six bulk binodals corresponding to the six two-phase regions as shown in Fig. 5 and 7, and as discussed above. The six bulk binodals translate into six sedimentation binodals in the stacking diagram in Fig. 8.

(2) Terminal lines: we have three terminal points of a binodal in the bulk phase diagram of this system:

- A triple point with Laves–fcc$_L$–fcc$_S$ phase coexistence.
- A triple point with Laves–fcc$_S$–fluid phase coexistence.
- A triple point with Laves–fcc$_L$–fluid phase coexistence.

The three terminal points appear as three terminal lines in the stacking diagram.

(3) Asymptotic terminal lines: similar to the q = 0.85 case, there are two binodals that involve a pure-component phase in

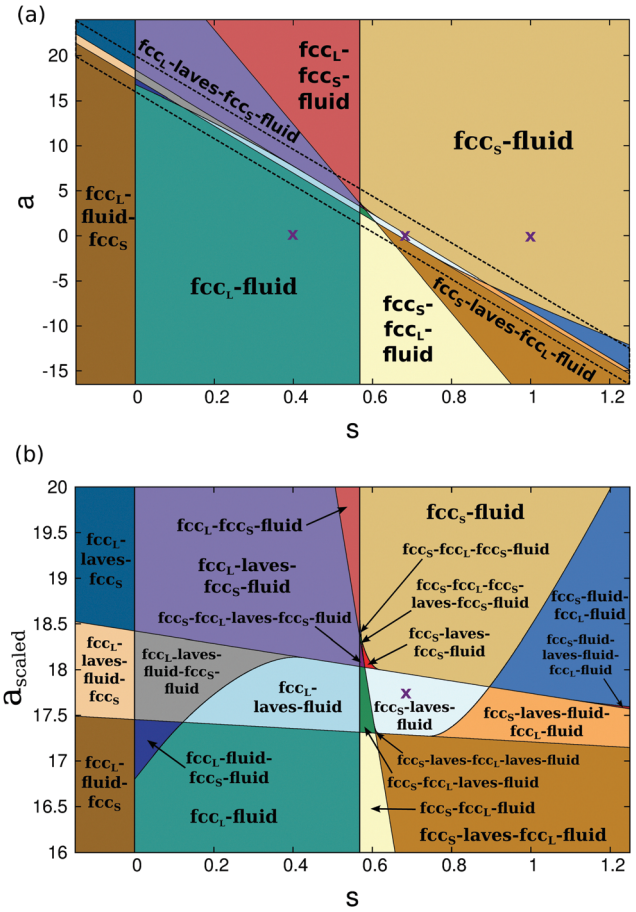

Fig. 8 (a) The stacking diagram for a binary mixture of hard spheres with a diameter ratio q = 0.82. The colored regions represent the different stacking sequences of phases observed in a sedimentation column. (b) Zoom-in of a rich section of the stacking diagram marked by a black dashed line in (a), where the a axis was linearly scaled with respect to s by a constant c for visualisation purposes. The new scaled $a_{scaled} = a - c \times s$ where $c = -26$. The purple crosses denote state points for EDBD simulations.

the bulk phase diagram. These correspond to vertical asymptotic terminal lines at $s = 0$ in the case that the pure phase consists of large spheres and at $s = -\infty$ if the pure phase contains only small spheres. The latter does not appear in the stacking diagram as it is beyond the scale of Fig. 8. For infinite pressures, the binary mixture demixes into two pure fcc phases with a finite slope of this asymptote in the μ_L–μ_S representation corresponding to a vertical line at $s \simeq 0.57$ in the SD of Fig. 8.

We note that the stacking diagram in Fig. 8 includes a region of negative s, which signifies that one species sediments while the other floats upward due to a negative buoyant mass. In this work, we assume that the large spheres always sediment signifying that its buoyant mass m_L is always positive. If the identity of the settling species for the case of negative s is reversed, then the phases in the stacking sequences in this region are simply reversed. Fig. 8 is primarily divided into four broad regions with respect to the value of gravitational variable s.

(1) $s < 0$: as mentioned above, a negative s implies that the large spheres sediment while the small spheres cream up. As a result the large species crystallize at the bottom of the column and the small spheres crystallize towards the top as their density and chemical potential increase in the direction opposite to gravity. At intermediate heights, the system forms a binary fluid phase, which crystallizes into a binary Laves phase at sufficiently high chemical potentials, *i.e.*, sufficiently high a.

(2) $0 < s < 0.57$: both species sediment in this regime. However the mass of the large species is higher and hence the large spheres sediment faster. As expected, at sufficiently high bulk chemical potentials (*i.e.* high concentrations), the large species crystallizes and forms an fcc phase at the base of the column. For low values of a, the fcc$_L$ crystal phase is followed by the fluid phase whereas for higher a values, crystalline phases such as the Laves or fcc$_S$ phase can form.

(3) $0.57 < s < 1$: this region may seem counterintuitive as the pure component phase formed at the bottom of the sedimentation column is that of the small species, whereas the large species is still the heavier species. However, the bulk chemical potentials, μ_S^0 and μ_L^0, are chosen such that it corresponds to the fcc$_S$ phase at the bottom of the column.

(4) $s > 1$: in this region, the smaller species is heavier and consequently, an fcc$_S$ forms at the bottom of the column.

3.5 Event-driven Brownian dynamics

In order to verify our theoretical predictions, we perform simulations at specific state points in the stacking diagram of Fig. 8. We perform EDBD simulations using the method as described in Section 2.3 on a binary mixture of 100 000 hard spheres with a diameter ratio q = 0.82 and number fraction x_S = 0.667. The cross-sectional area of the simulation box is $\simeq 50\sigma_L \times 50\sigma_L$. We set the gravitational length of the large spheres l_g^L to unity and test the gravitational length ratios $s = l_g^L/l_g^S$ = 0.4, 0.68 and 1.0. We assume that for these gravitational lengths the sedimentation is slow enough that the local density approximation is valid. We set the composition variable a as defined in eqn (8) by calculating the chemical potentials μ_L^0 and μ_S^0 in a bulk mixture without gravity using the Widom particle insertion method,[35] for the overall mixture composition and overall packing fraction of the sedimentation box as used in our simulations. The simulation state points (s,a) are marked with purple crosses in Fig. 8.

We first discuss our results for s = 0.4 and s = 1.0 (marked in Fig. 8(a)). The initial packing fraction in the column is 0.01. In Fig. 9, we present typical configurations of the sedimentation–diffusion equilibria observed. In Fig. 9(a) and (b), we color the larger spheres red and the smaller species green. We clearly observe that the crystal formed at the bottom of the sedimentation column consists predominately of large spheres at s = 0.4 and of small spheres at s = 1.0. This is further illustrated by Fig. 9(c) and (f) where we have plotted the species density profiles, $\rho_L(z)$ and $\rho_S(z)$, as a function of height z. The density profiles show discrete peaks at $z \leq 10\sigma_L$ which indicates layering. To analyze the crystallinity of the sediment, we use the q_6 bond order parameter[31,36] to determine whether a particle is solid-like or fluid-like. In Fig. 9(d) and (e), we color the solid-like particles with a darker shade than the fluid-like particles,

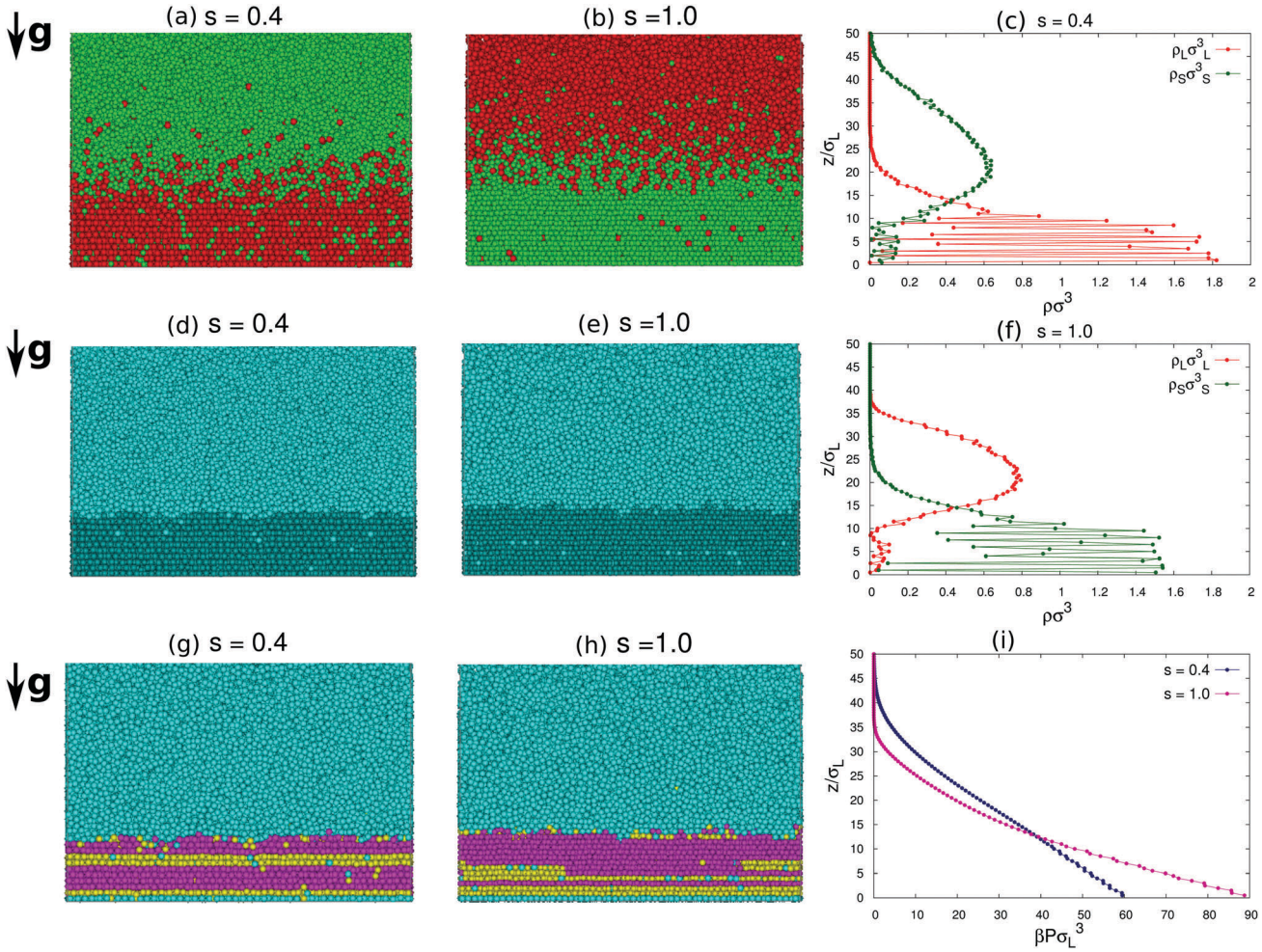

Fig. 9 Typical configurations of a sedimentation–diffusion equilibrium as obtained from EDBD simulations of a binary mixture of hard spheres with a diameter ratio $q = 0.82$ and a gravitational length ratio $s = l_g^L/l_g^S = 0.4$ (left) and 1.0 (right) with $l_g^L = 1$ at $t/\tau = 50\,000$. The state points of these simulations are shown as purple crosses in Fig. 8(a). (a and b) The particles are colored according to their size. Red denotes the large spheres and green represents the small spheres. (d and e) The particles are colored according to a q_6 bond order parameter analysis to distinguish the solid-like particles from the fluid-like particles. The solid-like particles are denoted by a darker shade of cyan than the fluid-like particles. (g and h) The particles are colored according to the crystal type. Magenta denotes fcc-stacked particles, yellow denotes hcp-stacked particles, cyan denotes the fluid-like particles. (c and f) Density profiles $\rho_{L/S}(z)$ of the two species as a function of the height z. (i) Pressure $\beta P(z)\sigma_L^3$ as a function of z.

which shows that the sediment at the bottom of the sample is crystalline. Then, using a 2D bond order analysis on the layers of the sediment[32] we identify that the crystalline sediment for $s = 0.4$ is a predominantly fcc-like crystal of large spheres in magenta with a few hexagonal-close-packed (hcp)-stacked particles colored in yellow (Fig. 9(g)), and an fcc crystal of small spheres with again a few hcp-stacked particles for $s = 1.0$ (Fig. 9(h)). The SD as presented in Fig. 8 shows that the fcc crystal formed at the bottom of the sedimentation column consists of large spheres, fcc_L, for $s < 0.57$, and of small spheres, fcc_S, for $s > 0.57$. Hence, our simulations are in excellent agreement with the theoretical predictions for $q = 0.82$. Interestingly, for $s = 1.0$, which signifies that both species sediment at the same rate, the smaller species forms an fcc crystal at the bottom of the column. Additionally, we calculate the pressure along the column by integrating the density profile along the direction of gravity. Fig. 9(i) shows the pressure profile in the column from which we find that the pressure $\beta P(z = 0)\sigma_L^3 \approx 60$ for $s = 0.4$ and ≈ 90 for $s = 1.0$. The pressure at the bottom of the column $\beta P(z = 0)\sigma_L^3$, where the gravitational potential equals 0, directly relates to the bulk phase diagram of Fig. 5. These values for the pressure correspond to the fcc_L–fcc_S coexistence region in Fig. 5, and one might naively expect to find a phase-separated fcc phase at the bottom of the sediment. However, from Fig. 7 it becomes evident that the crystal at this specific pressure value at the bottom of the sediment corresponds most probably to one of the pure fcc phases since only one unique combination $(\mu_L(x_S,P,T),\mu_S(x_S,P,T))$ corresponds to a point exactly on the binodal.

As the fcc phases crystallize in accordance with our theoretical predictions, we next attempt to self-assemble the Laves phase. This is a significant challenge when one considers that spontaneous self-assembly of the Laves phase has never been observed in bulk simulations of binary hard-sphere mixtures. We perform

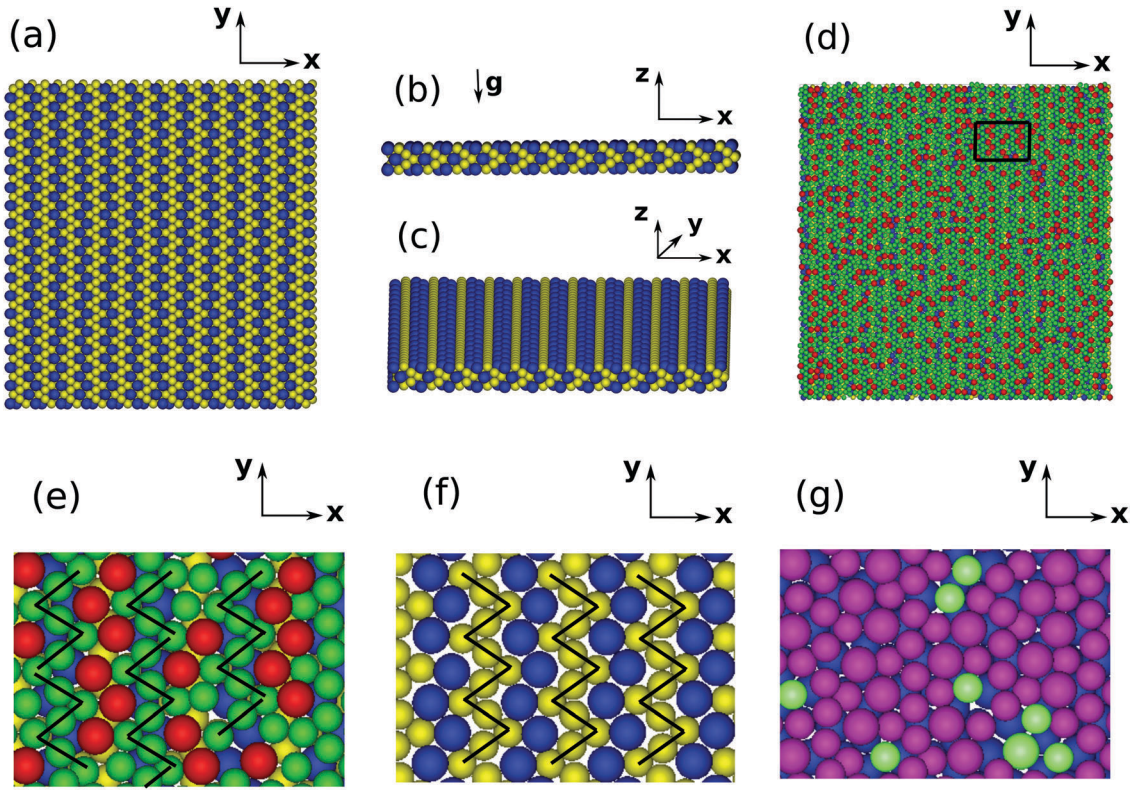

Fig. 10 Typical configuration of the first layer of a binary mixture of hard spheres with a diameter ratio $q = 0.82$ sedimenting on a $MgCu_2(110)$ template as obtained from EDBD simulations using a gravitational length ratio $s = l_g^L/l_g^S = 0.68$ with $l_g^L = 1$ at $t/\tau = 45\,000$. (a–c) Blue and yellow denote the large and small hard spheres of the template, respectively. (d and e) Red denotes the large spheres and green represent the small spheres of the sedimenting mixture (f) shows the ordering of the two species on the template. Black lines are used to highlight the patterning/ordering. (g) To indicate the substitutional ordering, the on-lattice species are colored in purple and the substitutionally ordered species are highlighted in fluorescent green.

simulations as before on a binary hard-sphere mixture for the following simulation parameters: $q = 0.82$, $x_S = 0.667$, $s = l_g^L/l_g^S = 0.68$. The initial overall packing fraction of the column is 0.1. This simulation state point is shown in Fig. 8 as a purple cross representing a specific point $(s,a) = (0.68,0.0537)$. The expected stacking sequence for this state point from bottom to top of the sedimentation column is fcc_S–Laves–fluid. We suspect that the formation of a binary crystal phase on top of a single-component fcc phase may be hampered by kinetic constraints. For example, the particles may get arrested in the holes of the fcc phase and may not have sufficient time to equilibrate to the Laves phase. Additionally there may be energetic constraints as the formation of an interface between two crystal phases can be energetically unfavorable. Therefore we truncate the stacking sequence and set the pressure to a lower value $\beta P(z = 0)\sigma_L^3 \simeq 30$ such that the phase at the bottom of the column corresponds to the Laves phase. Also keeping in mind that the interfacial tension between the smooth wall and the hexagonal geometry is the lowest among known geometries,[37] it is probable that the first layer in contact with the wall attempts to partially order into hexagonal order as the composition in the layer would be $x_S > 0.667$. In order to eliminate this possibility, we template the bottom wall with the (110) crosssection of the $MgCu_2$ crystal in accordance with the study by Hynninen *et al.*[13] The density that we choose for our template needs to be high enough to (i) restrain the incoming particles in-plane[32,38] and (ii) minimize substitutional ordering of species. However it should not be so high that there is a density mismatch between the first crystalline layer and the template[32] at $\beta P(z = 0)\sigma_L^3 \simeq 30$. Keeping these factors in mind the packing fraction of the $MgCu_2(110)$ template (shown in Fig. 10(a)–(c)) that we use is 0.656. In Fig. 10(d) we show the first layer of particles that sediment on the template. If we look closely at this layer, and zoom-in to the section enclosed within the black box (shown in Fig. 10(e)), we observe that the particles sit at the lattice positions in direct comparison with the template below. Interestingly, we observe that the first layer displays the characteristic ''six-bead'' ordering of the small species which is also typical of the $MgCu_2(110)$ template (Fig. 10(f)). We have highlighted these ''six-bead'' sequences formed by the small species by black lines. For exact comparison, we first draw these connecting black lines on the template, reproduce them unaltered in scale and orientation on Fig. 10(e), and subsequently shift them so that they approximately run through the center of the first layer particles. As a result of this, some order mismatches (*i.e.* tips of the black lines do not meet) are evident in the first layer. On closer inspection, these mismatches appear when there is substitutional ordering in the local environment. Substitutional ordering refers to spheres that sit at lattice positions irrespective of their identity, *i.e.*, a small sphere may be positioned on a large sphere lattice

location and *vice versa*. Also worth noting is that these six-bead small species arrangements stack on the larger species of the template, which is also commensurate with how the two species stack on a perfect $MgCu_2(110)$ template. This kind of stacking is particularly interesting when one considers that there are no interactions between the species and that the two species are very comparable in size (q = 0.82). We depict substitutional ordering in Fig. 10(g) by coloring the particles that sit at the right lattice positions in purple and those that are positioned at the wrong lattice positions in fluorescent green. From this figure, it is also clear that substitutional defects also result in an increase in the number of defects in their local environments, which hampers the formation of the Laves phase. We therefore suspect that short-ranged repulsive or attractive potentials may be required to better direct the self-assembly of the Laves phase on the template. We surmise that attractive interactions between unlike species[23] and/or repulsive interactions between like species may assist the ordering of the Laves phase during sedimentation on a template. We leave this for a future study.

4 Conclusions

To summarize, we have studied the sedimentation behavior of a binary mixture of hard spheres with a size ratio q for which the Laves phase is thermodynamically stable. We first construct the stacking diagram (SD) that describes the possible stacking sequences of stable phases in a sedimentation–diffusion equilibrium using the bulk phase diagram of the system in the chemical potential plane as input. We discuss in detail the features of the SD which delimit the regions representing unique phase stacking sequences, in relation to the corresponding bulk phase diagram. We calculate the SD for q = 0.85 for which the Laves phase is not stable, and for q = 0.82 for which the Laves phase is thermodynamically stable. We observe that the SD increases considerably in complexity with the entry of an extra stable phase in the bulk phase diagram. More specifically, the SD for q = 0.85 shows 7 unique stacking sequences in Fig. 4, whereas the SD for q = 0.82 shows 18 (+2, not shown) stacking sequences in Fig. 8. We also observe for both size ratios q stacking sequences that contain floating crystalline phases.

We then select specific state points in the SD for q = 0.82, and employ event-driven Brownian dynamics (EDBD) simulations to investigate the sedimentation behavior for a binary hard-sphere mixture in relation to our theoretical predictions. The first two simulation state points that we select for the purposes of comparison are (the ratio of buoyant masses s, the composition variable a) = (0.4,0.033) and (s,a) = (1.0, −0.025), in order to observe the reversal of the fcc phase that forms at the bottom of the sedimentation column. Our EDBD simulations indeed demonstrate that the large spheres crystallize at the bottom of the sediment into an fcc_L phase for s = 0.4, whereas the smaller spheres form the fcc_S phase at the bottom of the column for s = 1 in agreement with our stacking diagram.

As the ''reversal'' of the single-component fcc phase agrees with our theoretical predictions, we then attempt to self-assemble the Laves phase using EDBD simulations. We select the simulation parameters from a third state point in our SD which corresponds to the fcc_S–Laves–fluid phase stacking sequence from bottom to top in a sediment–diffusion equilibrium. In order to bypass the kinetic and energetic constraints in the formation of a binary crystal on top of a single-component fcc phase, we truncate the sedimentation path by setting the maximum pressure to $\beta P(z = 0)\sigma_L^3 \simeq 30$ so that the pressure at the bottom of the sediment corresponds to the desired Laves phase. Mindful of the fact that the interfacial tension of a hexagonal symmetry is the lowest with a smooth wall, we also template the bottom of the sedimentation column with the (110) plane of a $MgCu_2$ phase.[13] A closer inspection of the first layer that sediments on the template reveals the characteristic ''six-bead'' sequences of small spheres that are predominately stacked on top of the large species in the template. This is particularly interesting if one considers that there is no energetic interactions between the two species and the stacking arrangement is driven by entropy alone. Furthermore, the first layer of particles also displays substitutional ordering of species on the template *i.e.* spheres are positioned at lattice positions of the template irrespective of their identity. The occurrence of such a ''substitutional defect'' is seen to lead to an increase in local defects. From an entropic point of view, we expect that the Laves phase possesses a finite equilibrium concentration of substitutional defects. We leave the explicit calculations of the free energy as a function of the equilibrium defect concentration for future investigations. The presence of substitutional defects hinders further growth of the Laves phase. We postulate that short-ranged repulsive or attractive interactions may be required to direct the self-assembly of the Laves phase on the template. This will be studied in more detail in our next study.

Conflicts of interest

The authors declare no competing interests.

Acknowledgements

This work was done as part of the Industrial Partnership Programme, ''Computational Sciences for Energy Research'' (Grant no. 13CSER025), of the Netherlands Organization for Scientific Research (NWO). This programme is co-financed by Shell Global Solutions International B.V. TD thanks John R. Edison for useful discussions. The authors thank Chris L. Kennedy and Douglas R. Hayden for critical reading of the manuscript.

References

1 B. Alder and T. Wainwright, *J. Chem. Phys.*, 1957, **27**, 1208–1209.
2 P. N. Pusey and W. Van Megen, *Nature*, 1986, **320**, 340–342.
3 V. J. Anderson and H. N. Lekkerkerker, *Nature*, 2002, **416**, 811–815.
4 B. Li, D. Zhou and Y. Han, *Nat. Rev. Mater.*, 2016, **1**, 15011.
5 S.-Y. Lin, E. Chow, V. Hietala, P. R. Villeneuve and J. Joannopoulos, *Science*, 1998, **282**, 274–276.

6 J. Ge and Y. Yin, *Angew. Chem., Int. Ed.*, 2011, **50**, 1492–1522.
7 M. Wang and X. Wang, *Sol. Energy Mater. Sol. Cells*, 2008, **92**, 357–362.
8 E. Haugan, H. Granlund, J. Gjessing and E. S. Marstein, *Energy Procedia*, 2011, **10**, 292–296.
9 K. Busch and S. John, *Phys. Rev. E: Stat. Phys., Plasmas, Fluids, Relat. Interdiscip. Top.*, 1998, **58**, 3896.
10 K. Ho, C. T. Chan and C. M. Soukoulis, *Phys. Rev. Lett.*, 1990, **65**, 3152.
11 A. Garcia-Adeva, *New J. Phys.*, 2006, **8**, 86.
12 Y. A. Vlasov, B. Xiang-Zheng, J. C. Sturm and D. J. Norris, *Nature*, 2001, **414**, 289.
13 A.-P. Hynninen, J. H. Thijssen, E. C. Vermolen, M. Dijkstra and A. Van Blaaderen, *Nat. Mater.*, 2007, **6**, 202–205.
14 J. Perrin, *Brownian motion and molecular reality*, 1909.
15 R. Piazza, *Rep. Prog. Phys.*, 2014, **77**, 056602.
16 D. de las Heras and M. Schmidt, *Soft Matter*, 2013, **9**, 8636–8641.
17 D. de las Heras and M. Schmidt, *J. Phys.: Condens. Matter*, 2015, **27**, 194115.
18 M. Schmidt, M. Dijkstra and J.-P. Hansen, *Phys. Rev. Lett.*, 2004, **93**, 088303.
19 H. Pattabhiraman and M. Dijkstra, *J. Chem. Phys.*, 2017, **147**, 104902.
20 D. de las Heras, L. L. Treffenstädt and M. Schmidt, *Physical Review E*, 2016, **93**, 030601.
21 D. De Las Heras, N. Doshi, T. Cosgrove, J. Phipps, D. I. Gittins, J. S. Van Duijneveldt and M. Schmidt, *Sci. Rep.*, 2012, **2**, 789.
22 G. Avvisati, T. Dasgupta and M. Dijkstra, *ACS Nano*, 2017, **11**, 7702–7709.
23 É. Ducrot, M. He, G.-R. Yi and D. J. Pine, *Nat. Mater.*, 2017, **16**, 652–657.
24 A.-P. Hynninen, L. Filion and M. Dijkstra, *J. Chem. Phys.*, 2009, **131**, 064902.
25 G. Mansoori, N. Carnahan, K. Starling and T. Leland Jr, *J. Chem. Phys.*, 1971, **54**, 1523–1525.
26 R. J. Speedy, *J. Phys.: Condens. Matter*, 1997, **9**, 8591.
27 J. M. Polson, E. Trizac, S. Pronk and D. Frenkel, *J. Chem. Phys.*, 2000, **112**, 5339.
28 C. Vega, E. Sanz, J. Abascal and E. Noya, *J. Phys.: Condens. Matter*, 2008, **20**, 153101.
29 T. Drwenski, P. Hooijer and R. van Roij, *Soft Matter*, 2016, **12**, 5684–5692.
30 A. Scala, T. Voigtmann and C. De Michele, *J. Chem. Phys.*, 2007, **126**, 134109.
31 M. Marechal, M. Hermes and M. Dijkstra, *J. Chem. Phys.*, 2011, **135**, 034510.
32 T. Dasgupta, J. R. Edison and M. Dijkstra, *J. Chem. Phys.*, 2017, **146**, 074903.
33 T. Geigenfeind and D. de las Heras, *J. Phys.: Condens. Matter*, 2016, **29**, 064006.
34 L. Filion and M. Dijkstra, *Phys. Rev. E: Stat., Nonlinear, Soft Matter Phys.*, 2009, **79**, 046714.
35 D. Frenkel and B. Smit, *Understanding molecular simulation: from algorithms to applications*, Elsevier, 2001, vol. 1.
36 P. J. Steinhardt, D. R. Nelson and M. Ronchetti, *Phys. Rev. B: Condens. Matter Mater. Phys.*, 1983, **28**, 784.
37 M. Heni and H. Löwen, *Phys. Rev. E: Stat. Phys., Plasmas, Fluids, Relat. Interdiscip. Top.*, 1999, **60**, 7057.
38 K. Jensen, D. Pennachio, D. Recht, D. Weitz and F. Spaepen, *Soft Matter*, 2013, **9**, 320–328.